Origin of negative anisotropic magnetoresistance effect in math xmlns="http://www.w3.org/1998/Math/MathML">mrow>msub>mi>Fe/mi>mrow>mn>0.75/mn>/mrow>/msub>msub>mi>Co/mi>mrow>mn>0.25/mn>/mrow>/msub>/mrow>/math> single-crystal thin films upon Ir addition

Ryo Toyama, Satoshi Kokado, Keisuke Masuda, Zehao Li, Varun K. Kushwaha, Taisuke T. Sasaki, Loku Singgappulige Rosantha Kumara, Tomoyuki Koganezawa, Hiroo Tajiri, Takahiro Yamazaki, Masato Kotsugi, Yuma Iwasaki, and Yuya Sakuraba

Phys. Rev. Materials **7**, 084401 — Published 7 August 2023

DOI: 10.1103/PhysRevMaterials.7.084401

Origin of negative anisotropic magnetoresistance effect in $Fe_{0.75}Co_{0.25}$ single-crystal thin films upon Ir addition

Ryo Toyama,[1*] Satoshi Kokado,[2†] Keisuke Masuda,[1] Zehao Li,[1] Varun K. Kushwaha,[1] Taisuke T. Sasaki,[1] Loku Singgappulige Rosantha Kumara,[3] Tomoyuki Koganezawa,[3] Hiroo Tajiri,[3] Takahiro Yamazaki,[4] Masato Kotsugi,[4] Yuma Iwasaki,[5] and Yuya Sakuraba[1‡]

[1]*Research Center for Magnetic and Spintronic Materials (CMSM), National Institute for Materials Science (NIMS), 1-2-1 Sengen, Tsukuba, Ibaraki 305-0047, Japan*

[2]*Graduate School of Integrated Science and Technology, Shizuoka University, 3-5-1 Johoku, Naka, Hamamatsu, Shizuoka 432-8561, Japan*

[3]*Japan Synchrotron Radiation Research Institute (JASRI), SPring-8, 1-1-1 Kouto, Sayo, Hyogo 679-5198, Japan*

[4]*Faculty of Advanced Engineering, Tokyo University of Science, 6-3-1 Niijuku, Katsushika, Tokyo 125-8585, Japan*

[5]*Center for Basic Research on Materials (CBRM), National Institute for Materials Science (NIMS), 1-1 Namiki, Tsukuba, Ibaraki 305-0044, Japan*

[*]TOYAMA.Ryo@nims.go.jp

[†]kokado.satoshi@shizuoka.ac.jp

[‡]SAKURABA.Yuya@nims.go.jp

Anisotropic magnetoresistance (AMR) effect is one of the fundamental spin-dependent transport phenomena in ferromagnets and has been the subject of numerous experimental observations. However, the origin of AMR including the sign change of the magnetoresistance has not been fully clarified theoretically. In this study, we observe a large negative AMR ratio in $Fe_{0.75}Co_{0.25}$ single-crystal thin films upon Ir addition and elucidate its origin by a theoretical model. $(Fe_{0.75}Co_{0.25})_{100-x}Ir_x$ composition-spread thin films with x up to 11% are fabricated on MgO(100) substrates by combinatorial sputtering technique. From X-ray diffraction (XRD) results, metastable $B2$-ordered phase of Fe_3Co–Ir is detected from x = 2.1%, which does not appear in the bulk equilibrium phase diagram. The $B2$-ordering is also confirmed by scanning transmission electron microscope. The AMR ratio of the pure Fe_3Co shows a small positive value of 0.3%. In contrast, once the Ir atoms are added, the AMR ratio becomes negative, and it exhibits the largest negative values of –4.7% at 10 K and –3.6% at 300 K for x = 11%. Using a theoretical model, the sign change of AMR ratio from positive to negative upon $B2$-ordering is obtained for high Ir concentration, which agrees with the experimental results. Thus, the metastable $B2$-ordering would be the key to observing the negative AMR. These findings provide a deep insight into the origin of AMR in heavy-metal-doped ferromagnetic ordered alloys.

□. INTRODUCTION

The anisotropic magnetoresistance (AMR) effect in ferromagnetic 3*d* transition metals and alloys has been studied extensively from the fundamental and applied points of view since its discovery about 170 years ago [1–14]. The AMR effect is one of the representative spin-dependent transport phenomena induced by spin–orbit coupling, in which the electrical resistivity in a ferromagnet depends on the relative angles between the current and magnetization directions [1–3]. Most of the typical ferromagnets such as Fe–Co binary alloys show a positive AMR ratio, where the resistivity is larger when the current and magnetization directions are parallel than that when they are orthogonal [1–14]. To modulate the output signals of AMR, the effect of doping third elements including various 4*d* and 5*d* heavy metals such as Pd and Pt has been widely reported [15–22]. Especially, the combination of ferromagnetic 3*d* transition metals and the heavy metals often produce ordered alloys such as $L1_0$ and $L1_2$ phases, and the relationship between the ordering and AMR ratio has been explored [23–29].

The negative sign of AMR ratio upon heavy metal addition into 3*d* transition metals and alloys has also been observed experimentally [1, 30–32]. For example, $Ni_{96.1}Ir_{3.9}$ showed a negative AMR ratio of –1.52% at 4.2 K [30]. The room temperature negative AMR ratio was observed in Ir-doped Fe, Ni, Co, Fe_2Ni_8, and Co_3Ni_7 as well as at low temperatures, and the largest value of –2.56% was observed in $Co_{97}Ir_3$ [31]. In addition, negative AMR ratio up to approximately –2.7% was observed in NiPd alloys at 1.5 K [32].

As described above, many experimental studies on the AMR effect have been reported. However, the mechanism of AMR effect including its sign change in ferromagnetic 3*d* transition metals and alloys upon heavy metal addition has not been revealed in detail theoretically.

In this study, we observe a large negative AMR ratio in $Fe_{0.75}Co_{0.25}$ single-crystal thin films upon Ir addition and elucidate the origin of the negative AMR effect by a theoretical model. We fabricate $(Fe_{0.75}Co_{0.25})_{100-x}Ir_x$ composition-spread thin films with x up to 11% on MgO(100) substrates using a combinatorial deposition technique and measure the compositional dependence of AMR. The combinatorial deposition technique is one of the most effective ways to investigate the transport properties as well as the structural properties [33–39]. Using a composition-spread film, where the atomic composition changes continuously within one sample, enables high-throughput measurement and precise evaluation of AMR properties without the error caused by making individual samples with different composition ratio because all target compositions exist within a single identical sample. In addition, using single-crystal films is easier to characterize the structural and physical properties than using polycrystal samples. Thus, the fabrication of $(Fe_{0.75}Co_{0.25})_{100-x}Ir_x$ single-crystal composition-spread films is beneficial. From the structural analysis, metastable *B*2-ordered phase of Fe_3Co–Ir is detected in the films with x from 2.1%, which does not appear in the bulk equilibrium phase diagram of Fe–Co–Ir ternary alloys. From the transport measurement, the AMR ratio changes from a small positive to a large negative by Ir addition, and the largest negative values of –4.7% at 10 K and –3.6% at 300 K are observed at maximum Ir concentration. From the theoretical analysis, the sign change of AMR ratio from positive to negative upon *B*2-ordering is obtained for high Ir concentration, which agrees with the experimental results. Based on these observations, we conclude that the metastable *B*2-ordering would

be the key to observing the negative AMR.

□. METHODS

A. Fabrication

$(Fe_{0.75}Co_{0.25})_{100-x}Ir_x$ composition-spread films with x designed to be up to 10% were fabricated on single-crystal MgO(100) substrates (Furuuchi Chemical Corp.) using a combinatorial sputtering system (CMS-A6250X2, Comet Inc.). The schematic diagram of the film is illustrated in Fig. 1(a). Prior to deposition, MgO(100) substrates were subjected to ultrasonication cleaning using acetone, ethanol, and deionized water. The substrates were further cleaned by Ar-ion milling in a vacuum chamber. The deposition was performed with a substrate temperature of room temperature and a process Ar gas pressure of 0.8 Pa. A uniform $Fe_{0.75}Co_{0.25}$ layer with 0.44 nm in thickness was firstly deposited on the substrates by RF magnetron co-sputtering of individual Fe and Co targets. The sputtering power for Fe and Co was tuned so that the composition ratio of Fe to Co was 3 to 1. Then, a wedge-shaped $Fe_{0.75}Co_{0.25}$ layer with 0.00 to 0.06 nm in thickness was deposited in 7 mm width region by the co-sputtering using a linear moving shutter. After that, the substrates were rotated by 180° and a wedge-shaped Ir layer with the same thickness was deposited on the wedge-shaped Fe_3Co layer by DC magnetron sputtering. Thus, the total thickness of one unit of $Fe_{0.75}Co_{0.25}$–Ir layer was 0.5 nm with a flat surface. The deposition rates for $Fe_{0.75}Co_{0.25}$ and Ir were 0.0146 and 0.0108 nm/s, respectively. This deposition process was repeated 60 times. Finally, 30-nm-thick $(Fe_{0.75}Co_{0.25})_{100-x}Ir_x$ composition-spread films were obtained. After the deposition, the films were annealed in a vacuum for 30 min with a maximum attainable temperature of approximately 380 °C to make a homogeneous composition distribution with respect to the normal direction of the film surface. After cooling, a Ru cap layer with 2 nm in thickness was deposited on the films to prevent oxidization.

The actual composition ratios for pure $Fe_{0.75}Co_{0.25}$ and Ir-rich regions of the films were $Fe_{0.754}Co_{0.246}$ and $(Fe_{0.761}Co_{0.239})_{89.0}Ir_{11.0}$, respectively, which were determined by X-ray fluorescence (ZSX Primus □, Rigaku). Hereafter, we denote $Fe_{0.754}Co_{0.246}$ and $(Fe_{0.761}Co_{0.239})_{89.0}Ir_{11.0}$ as Fe_3Co and $(Fe_3Co)_{89}Ir_{11}$, respectively.

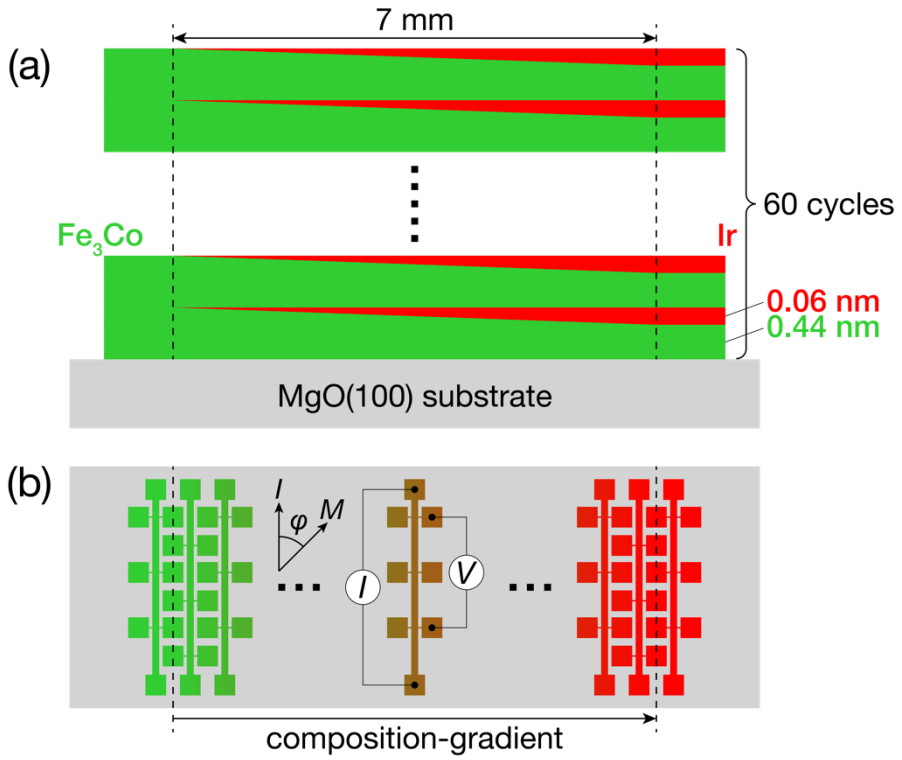

FIG. 1. Schematic diagrams of $(Fe_{0.75}Co_{0.25})_{100-x}Ir_x$ composition-spread thin films and multi-terminal devices on MgO(100) substrates. (a) Side-view of the composition-spread film. The one unit layer of 0.5 nm consists of a uniform $Fe_{0.75}Co_{0.25}$ layer of 0.44 nm (green) and wedge-shaped $Fe_{0.75}Co_{0.25}$ (green) and Ir (red) layers of 0.06 nm with the composition-gradient width of 7 mm. The deposition of the one unit layer was repeated 60 times. Thus, the total film thickness was designed to be 30 nm. The actual composition ratios for pure $Fe_{0.75}Co_{0.25}$ and Ir-rich regions of the films were $Fe_{0.754}Co_{0.246}$ and $(Fe_{0.761}Co_{0.239})_{89.0}Ir_{11.0}$, respectively, which were determined by X-ray fluorescence. Hereafter, we denote $Fe_{0.754}Co_{0.246}$ and $(Fe_{0.761}Co_{0.239})_{89.0}Ir_{11.0}$ as Fe_3Co and $(Fe_3Co)_{89}Ir_{11}$, respectively. (b) Top-view of the multi-terminal devices patterned on the composition-spread film, which are perpendicular to the composition-gradient. The relative angle between the current (I) and magnetization (M) directions is denoted as φ.

B. Characterization

The compositional dependence of crystal structures of the composition-spread films was measured by laboratory X-ray diffraction (XRD; SmartLab, Rigaku) with Cu-$K\alpha$ (λ = 1.5418 □). The irradiation position of X-ray, which was collimated using a 0.5 mm incident slit, was changed in 1 mm step along the composition-gradient. A flat imaging plate was used to collect two-dimensional (2D) XRD images. The out-of-plane and tilted-plane XRD were measured with $\chi = 0°$ and 54.7°, respectively. The one-dimensional (1D) XRD patterns were obtained from the 2D XRD images using an instrument software (SmartLab Studio □, Rigaku). The degree of $B2$ order (S_{B2}) is estimated using the following equation:

$$S_{B2} = \sqrt{\frac{I_{100}^{exp}/I_{200}^{exp}}{I_{100}^{sim}/I_{200}^{sim}}} \quad (1)$$

where $I^{exp}_{100\ (200)}$ is the experimental integrated intensity of *100* superlattice (*200* fundamental) peak and $I^{sim}_{100\ (200)}$ is the simulated intensity of *100* (*200*) peak. The $I^{sim}_{100\ (200)}$ value is obtained using VESTA [40]. The crystal structures of the films were also measured by synchrotron XRD using the versatile six-axis diffractometer installed at the beamline BL13XU experimental hatch 1 of SPring-8, Japan. The photon energy of X-ray was set to 8.04 and 7.11 keV, which corresponds to Cu-*Kα* radiation and the absorption edge of Fe-*K*, respectively.

The cross-sectional high-angle annular dark-field scanning transmission electron microscope (HAADF-STEM) images, energy dispersive X-ray spectroscopy (EDS) elemental maps, and nano-beam electron diffraction (NBED) patterns of the region with x = 11% were taken and analyzed using an aberration-corrected STEM (FEI Titan G2 80-200, FEI Company). Thin foil for the STEM observation was prepared by the standard lift-out technique using FEI Helios G4 UX.

To evaluate AMR effect, the composition-spread films were patterned into multi-terminal devices, which was perpendicular to the composition-gradient, as illustrated in Fig. 1(b), using conventional photolithography and Ar-ion milling techniques. The width of the devices was designed to be 100 μm, so the compositional variation within one device was estimated to be approximately 0.14–0.15%. The compositional dependence of AMR effect was measured using Physical Property Measurement System (PPMS DynaCool, Quantum Design) with a sample rotator. The measurement temperature was varied from 10 to 300 K. During the measurement, a constant current (I) of 100 μA was applied to the <110> direction of the films, and a constant external magnetic field of 1 T, which was enough to saturate the magnetization (M) of the films, was rotated within the in-plane direction of the films. The relative angle between the I and M directions was denoted as φ. AMR ratio was defined as $(\rho_{\parallel}-\rho_{\perp})/\rho_{\perp}$, where $\rho_{\parallel}$ ($\rho_{\perp}$) is the resistivity of the films where φ = 0° (90°).

C. Theoretical calculation

The AMR ratios of *A*2-disordered Fe_3Co, *A*2-disordered $(Fe_3Co)_{89}Ir_{11}$, and *B*2-ordered $(Fe_3Co)_{89}Ir_{11}$ were calculated using the electron scattering theory developed by Kokado *et al*, which considers *s–d* scattering of conduction electrons from *s* to *d* orbitals and crystal field in the *d* orbitals of the matrix material under a two-current model [41]. The AMR ratio is expressed as [41–43]

$$AMR^{[110]} = 2C_2^{[110]} \tag{2}$$

$$C_2^{[110]} = \frac{3}{8}\frac{1}{1+r+\frac{3}{4}r_{s,-\to\varepsilon,-}+\frac{1}{4}r_{s,-\to\gamma,-}}\left\{\frac{1}{r+\frac{3}{4}r_{s,-\to\varepsilon,-}+\frac{1}{4}r_{s,-\to\gamma,-}}\left[\left(\frac{\lambda}{\Delta}\right)^2\left(r_{s,-\to\varepsilon,-}-r_{s,-\to\gamma,-}\right)-\frac{\lambda^2}{H\Delta}r_{s,-\to\varepsilon,-}+\right.\right.$$
$$\left.\left.\frac{\lambda^2}{\Delta(H+\Delta)}r_{s,-\to\gamma,-}\right]+\frac{\lambda^2}{H(H-\Delta)}r_{s,+\to\varepsilon,-}\left(r+\frac{3}{4}r_{s,-\to\varepsilon,-}+\frac{1}{4}r_{s,-\to\gamma,-}\right)\right\} \tag{3}$$

The λ is the spin–orbit coupling constant, H is the exchange field, and Δ is the energy difference between the ε and γ orbitals of *d* states. The r, $r_{s,+\to\varepsilon,-}$, $r_{s,-\to\varepsilon,-}$, and $r_{s,-\to\gamma,-}$ are expressed as $r=\frac{\rho_{s,-}}{\rho_{s,+}}=\left(\frac{m_-^*}{m_+^*}\right)^4\left(\frac{D_+^{(s)}}{D_-^{(s)}}\right)^2$, $r_{s,+\to\varepsilon,-}=\frac{\rho_{s,+\to\varepsilon,-}}{\rho_{s,+}}=\frac{\beta_+ D_{\varepsilon,-}^{(d)}}{D_+^{(s)}}$, $r_{s,-\to\varepsilon,-}=\frac{\rho_{s,-\to\varepsilon,-}}{\rho_{s,+}}=\frac{r\beta_- D_{\varepsilon,-}^{(d)}}{D_-^{(s)}}$, $r_{s,-\to\gamma,-}=\frac{\rho_{s,-\to\gamma,-}}{\rho_{s,+}}=\frac{r\beta_- D_{\gamma,-}^{(d)}}{D_-^{(s)}}$,

with $\beta_\sigma = \frac{n_{imp}N_n|V_{s\sigma\to d\sigma}|^2}{n_{imp}\left|V_s^{imp}\right|^2+\left|V_s^{ph}\right|^2}$, where r is the resistivity ratio of the s–s scattering for spin-down to that for spin-up, $r_{s,\sigma\to m,-} = \frac{\rho_{s,\sigma\to m,-}}{\rho_{s,+}}$ is the resistivity ratio of the s–d scattering resistivity of the s state with σ spin to the m orbit with spin-down against the s–s scattering resistivity for spin-up, $D_{m,\sigma}^{(n)}$ is the partial density of states (PDOS) of the wave function of the tight-binding model for the n state of the m orbital with σ spin at the Fermi energy (E_F), m_σ^* is the effective mass of the conduction electrons of the σ spin, β_σ is the uncertainty parameter for the σ spin depending on impurities and phonons, n_{imp} is the number density of impurities, N_n is the number of nearest-neighbor host atoms around a single impurity, $V_{s\sigma\to d\sigma}$ is the scattering potential due to a non-magnetic impurity in s–d scattering, and V_s^{imp} and V_s^{ph} are the scattering potentials due to a single impurity and phonon in s–s scattering, respectively [42].

To estimate the variable values in Eq. (3), PDOS of $A2$-disordered Fe_3Co, $A2$-disordered $(Fe_3Co)_{89}Ir_{11}$, and $B2$-ordered $(Fe_3Co)_{89}Ir_{11}$ were calculated on the basis of the density-functional theory and the Korringa–Kohn–Rostoker (KKR) method [44,45], implemented in the Akai-KKR code [46]. Here, the spin–orbit interaction was taken into account and the exchange-correlation energy was treated within the generalized gradient approximation [47]. The Brillouin-zone integration was performed with 15 × 15 × 15 k points for the self-consistent-field calculation and 20 × 20 × 20 for the PDOS calculation. The lattice constant and site occupancies for the three structures used for the calculation are listed in Table S□.

□. RESULTS AND DISCUSSION

A. Structural analysis

The 1D XRD patterns of the $(Fe_3Co)_{100-x}Ir_x$ composition-spread thin films for the $\chi = 0°$ and 54.7° measurements are shown in Figs. 2(a) and 2(b), respectively. The 2D XRD images of the films are also shown in Fig. S1 in the Supplemental Material [48].

From the 2D XRD images (Fig. S1 [48]), the all diffraction peaks observed in the composition-spread films were spot-like shapes, indicating that the films were (100)-oriented single-crystals and grown epitaxially on the single-crystal MgO(100) substrates for all Ir concentrations.

From the $\chi = 0°$ measurement [Fig. 2(a)], in the region without Ir, the fundamental peak of body-centered cubic (bcc) Fe_3Co *200* was observed at $2\theta = 65.18°$, corresponding to the lattice constant (a) of 2.862 □. This a value agrees with that of Fe_3Co in the literature [49]. As increasing the Ir concentration, the *200* peak clearly shifted to the lower diffraction angles, which means that the a value increased as increasing the Ir concentration owing to the larger atomic radius of Ir compared to that of Fe and Co. This indicates that the doped Ir was incorporated into the bcc Fe_3Co lattice. From $x = 6.4\%$, in addition to the fundamental peak, the superlattice peak corresponding to Fe_3Co–Ir *100* started to be observed at low a diffraction angle, indicating that the emergence of metastable $B2$-ordered phase. It should be noted that the $B2$-ordered phase of Fe_3Co–Ir does not appear in the bulk equilibrium phase diagram of Fe–Co–Ir ternary alloys [50] and has not been reported previously. When x = 11%, the

diffraction angle for the superlattice peak of *100* was $2\theta = 30.82°$, which corresponds to $a = 2.901$ □. The Ir concentration dependence on a derived from the *200* peak is summarized in Fig. 2(c).

From the $\chi = 54.7°$ measurement [Fig. 2(b)], the same trend of decreasing diffraction angle of the fundamental *200* peak with increasing Ir concentration was observed for the fundamental *222* peak. The superlattice peak of Fe_3Co–Ir also started to be observed from $x = 6.4\%$ as *111* peak at $2\theta \approx 55°$, indicating the *B*2-ordering of Fe_3Co–Ir. If there is a higher atomic order in 1*b* site (1/2, 1/2, 1/2) of bcc lattice between Fe/Co and Ir atoms forming $D0_3$-ordered structure, the size of unit cell becomes twice of that of *B*2-ordered structure and another superlattice peak of *111* is expected to appear at $2\theta \approx 24°$. The absence of the additional superlattice peak of *111* in Fig. 2(b) clearly suggests the formation of only *B*2-ordered structure in the $(Fe_3Co)_{100-x}Ir_x$ composition-spread film.

The Ir concentration dependence on S_{B2} estimated using Eq. (1) is shown in Fig. 1(d). The $I^{sim}_{100\ (200)}$ value in Eq. (1) was obtained for individual Ir concentrations by considering that all Ir atoms occupy the 1*b* site (1/2, 1/2, 1/2) in *B*2-ordered structure. The S_{B2} value increased from 0.57 to 0.82 as increasing the Ir concentration from 6.4% to 11%.

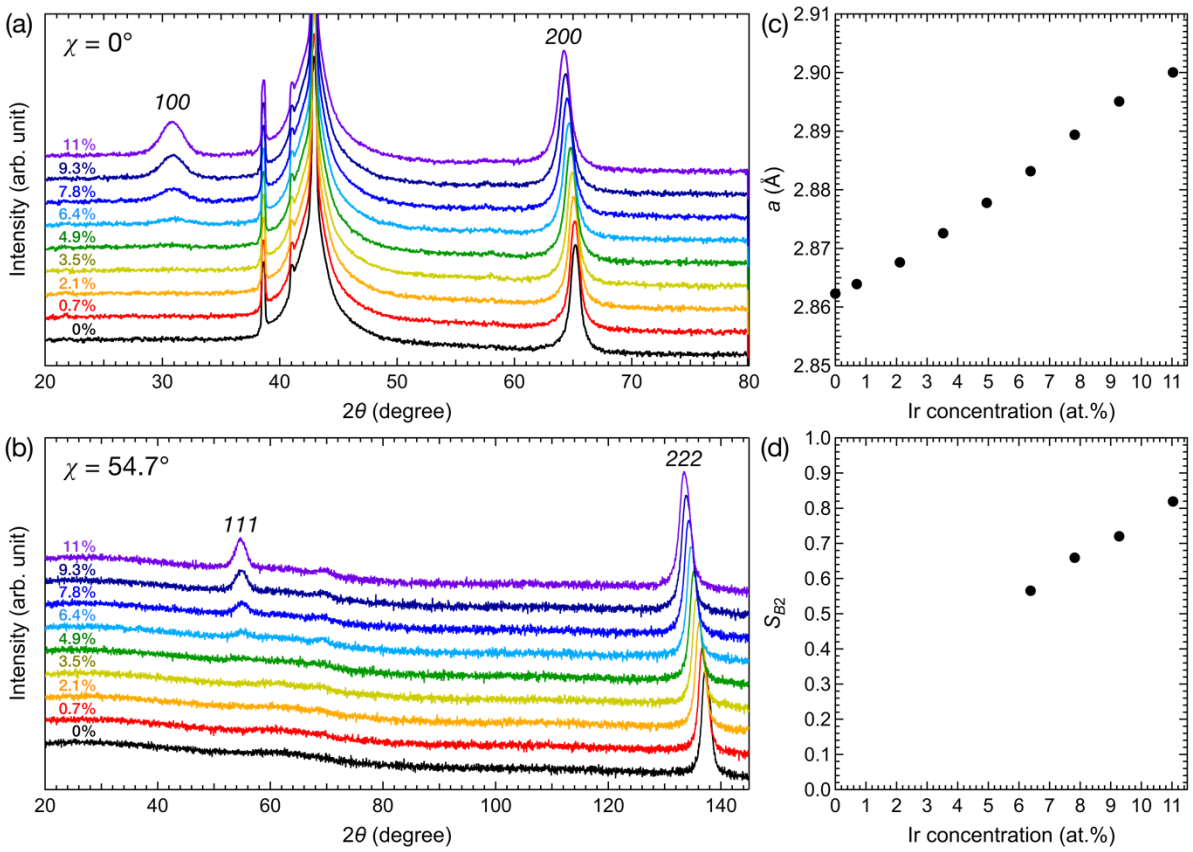

FIG. 2. Compositional dependence on one-dimensional (1D) X-ray diffraction (XRD) patterns of $(Fe_3Co)_{100-x}Ir_x$ composition-spread thin films with (a) $\chi = 0°$ and (b) 54.7° measurement configurations. Compositional dependences on (c) lattice constant (a) derived from *200* peak and (d) the degree of *B*2 order (S_{B2}).

The *B*2-ordered phase was not detected in the regions with x lower than 6.4% by the laboratory

XRD system as shown in Fig. 2, which can be due to the low brightness of the incident beam. To confirm whether the *B*2-ordered phase exists in the regions with lower Ir concentrations, the diffraction patterns of the regions with x lower than 6.4% were measured by synchrotron XRD with $\chi = 0°$. From Fig. 3, the superlattice peak of Fe_3Co–Ir *100* was observed at x = 2.1–4.9%, indicating that the *B*2-ordered phase was also formed at x = 2.1–4.9%.

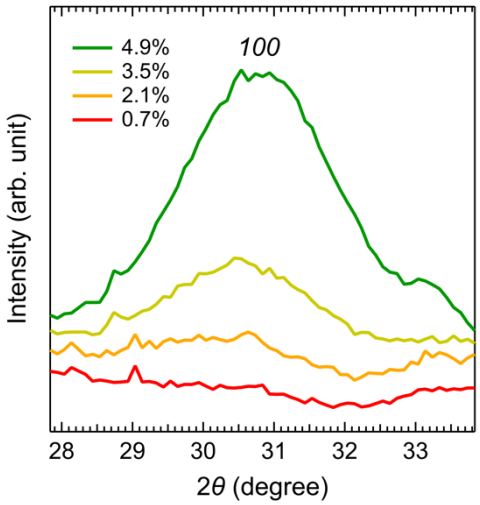

FIG. 3. Synchrotron XRD patterns of the regions with x = 0.7–4.9% with χ = 0° measurement configuration.

Furthermore, synchrotron XRD pattern of the region with x = 0% (Fe_3Co without Ir) was measured with a photon energy corresponding to the absorption edge of Fe-*K* (7.11 keV). As a result, superlattice peak of *100* was not observed (Fig. S2 [48]), which indicates that the *B*2-ordered phase was not form in the pure Fe_3Co. In other words, *B*2-ordered phase was formed only in the Ir-added region.

The cross-sectional HAADF-STEM image, EDS elemental maps, and EDS line scan of the region with x = 11% are shown in Fig. 4. From the EDS elemental maps [Fig. 4(b)], Fe (green), Co (light blue), and Ir (red) atoms were found to be distributed uniformly within the film, suggesting that there was no phase separation. The EDS line scan also showed uniform elemental distribution without inter-layer diffusion for each element along the cross-sectional direction [Fig. 4(c)].

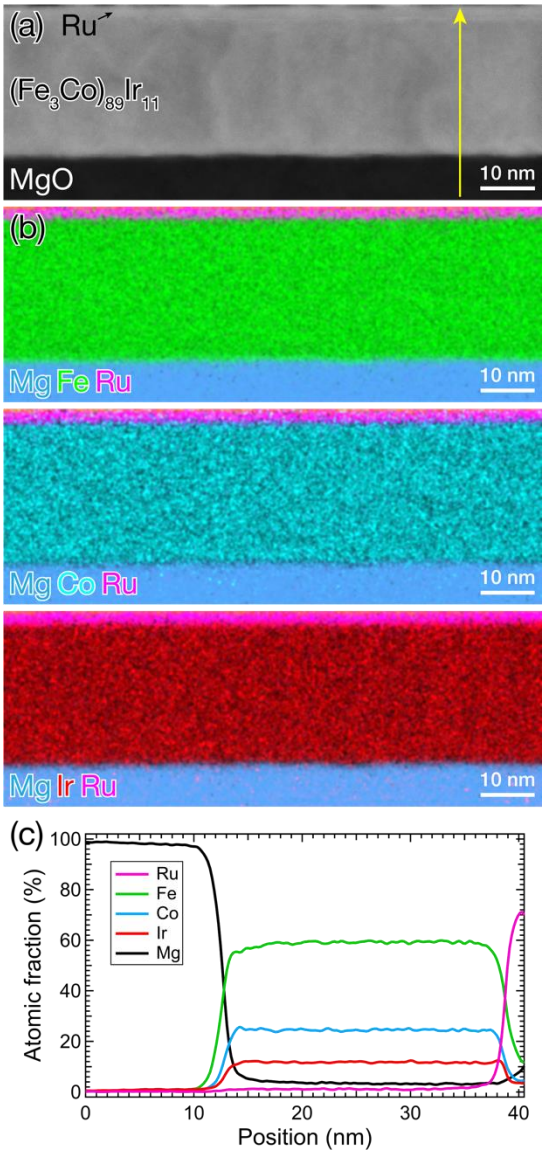

FIG. 4. (a) Cross-sectional high-angle annular dark-field scanning transmission electron microscope (HAADF-STEM) image, (b) energy dispersive X-ray spectroscopy (EDS) elemental maps of Mg (dark light blue), Fe (green), Co (light blue), Ir (red), and Ru (pink), and (c) EDS line scan of the region with x = 11% [$(Fe_3Co)_{89}Ir_{11}$]. The direction of EDS line scan is indicated by the yellow arrow in part (a).

The high-resolution HAADF-STEM image of the region with x = 11% is shown in Fig. 5(a). Note that the HAADF-STEM image was taken from the zone axis of [110] of $(Fe_3Co)_{89}Ir_{11}$. From the NBED pattern [Fig. 5(b)], the superlattice peaks of *001* were observed together with the fundamental peaks of *002*. This indicates the [001]-oriented epitaxial growth and the *B*2-ordering of Fe_3Co–Ir. These observations are consistent with the XRD results as shown in Fig. 2.

The high-magnification EDS elemental map is shown in the inset of Fig. 5(a). The atomic columns were resolved in some of the areas. From the EDS map [inset of Fig. 5(a)], the Fe- (green) and Ir-columns (red) tended to be arranged alternatively towards the [002] direction. The EDS line scan in the [002] direction [indicated by the white arrow in the inset of Fig. 5(a)] is shown in Fig. 5(c). It is clearly found that the Ir-column tended to occupy the Co-column. Namely, the Fe atoms occupied the 1*a* sites

(0, 0, 0) of the *B*2-ordered lattice, while the Co atoms occupied the 1*b* sites (1/2, 1/2, 1/2). Ir atoms (red) tended to occupy the Co (1*b*) sites (light blue) preferentially. Based on the EDS results, an ideal metastable *B*2-ordered Fe_3Co–Ir structure was determined as illustrated in Fig. 5(d), where the 1*a* site is occupied only by Fe atoms and the 1*b* site is occupied by the remaining Fe, Co, and Ir atoms.

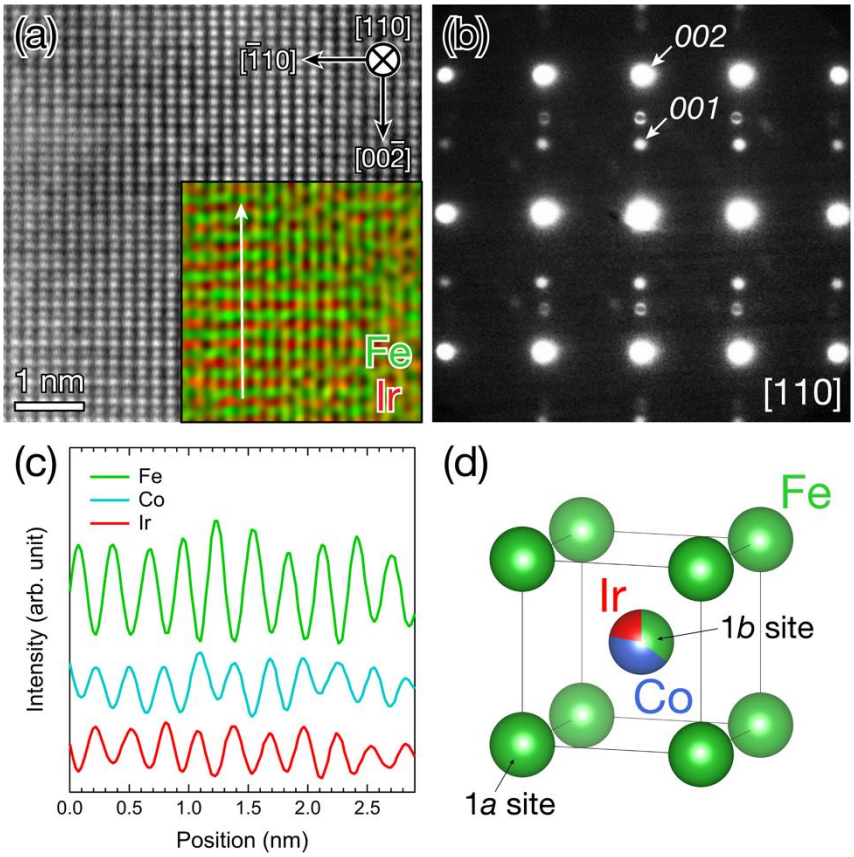

FIG. 5. Cross-sectional (a) high-resolution HAADF-STEM image and (b) nano-beam electron diffraction (NBED) pattern of the region with x = 11% [$(Fe_3Co)_{89}Ir_{11}$], which are taken from the zone axis of [110] of $(Fe_3Co)_{89}Ir_{11}$. The inset in part (a) shows the high-magnification EDS elemental map of Fe (green) and Ir (red). (c) EDS line scan in the [002] direction, which is indicated by the white arrow in the inset in part (a). (d) A schematic illustration of ideal metastable *B*2-ordered Fe_3Co–Ir structure determined by the EDS elemental maps. The Fe atoms occupied the 1*a* sites (0, 0, 0), while the remaining Fe, Co, and Ir atoms occupied the 1*b* sites (1/2, 1/2, 1/2).

B. Anisotropic magnetoresistance (AMR) effect

The temperature dependence on AMR of the $(Fe_3Co)_{100-x}Ir_x$ composition-spread thin films with x = 0% and 11% are shown in Figs. 6(a) and 6(b), respectively. For pure Fe_3Co (without Ir) [Fig. 6(a)], the AMR ratio was a positive value as small as 0.3%. The fourfold symmetry of AMR was observed for all temperature. The fourfold symmetry of AMR has also been reported in $Fe_{0.5}Co_{0.5}$ single-crystal thin films with I parallel to [110] direction [14]. When x = 11% [Fig. 6(b)], clear temperature-dependent negative AMR curves were observed with typical twofold symmetry. At 10 K, the negative AMR ratio was –4.7%, and this negative AMR persisted even at 300 K, with the AMR ratio of –3.6%. To the best,

these negative AMR ratios are the largest values so far among the heavy-metal-doped 3*d* transition alloys [1, 30–32].

The compositional dependence on AMR of the films measured at 10 and 300 K is shown in Fig. 6(c). Once the Ir atoms were added, the AMR ratio became negative, and it decreased as increasing the Ir concentration. The AMR ratio started to saturate from x = 6.4%, and it exhibited the maximum negative values of –4.7% at 10 K and –3.6% at 300 K for x = 11%.

The fourfold symmetry of AMR was observed for x = 0% [Fig. 6(a)], whereas typical twofold symmetry was observed for x = 11% [Fig. 6(b)]. However, the twofold and fourfold symmetry of AMR could coexist [41]. We roughly estimated the contribution of twofold and fourfold symmetry to the overall AMR curves for x = 0% and 11% measured at 10 K using the expression $AMR^{[110]}(\varphi) = C_2(1+\cos 2\varphi) + C_4(-1+\cos 4\varphi)$ [41]. As a result, $C_2 \approx 0.14\%$ and $C_4 \approx 0.14\%$ for x = 0% and $C_2 \approx -2.3\%$ and $C_4 \approx -0.03\%$ for x = 11%. For x = 0%, because the C_2 and C_4 values are comparable, the contribution of fourfold symmetry can be observable, as shown in Fig. 6(a). In contrast, for x = 11%, because the C_4 value was much smaller than C_2, the contribution of fourfold symmetry was not visible, and thus, the twofold symmetry was dominant [Fig. 6(b)].

In addition, based on the electron scattering theory, it was revealed that C_4 component appears in the tetragonal symmetry system where $d\varepsilon$ and/or $d\gamma$ orbitals has different DOS [41]. From the XRD results (Fig. 2), the c/a ratio (ratio of lattice constant for c-axis to a-axis) for x = 0% and 11% was found to be 0.997. In other words, Fe_3Co and $(Fe_3Co)_{89}Ir_{11}$ had tetragonal distortion ($|a–c|/a$) of 0.3%. Although this distortion value itself was small, the value was close to that of Fe_4N in the previous study (0.2%) [51]. For Fe_4N, C_4 and C_2 components were observed in in-plane AMR and transverse AMR, respectively, which were considered to be due to the tetragonal distortion [51–53]. Thus, the C_4 component for x = 0% and 11% in the in-plane AMR of this study would be attributed to the small tetragonal distortion.

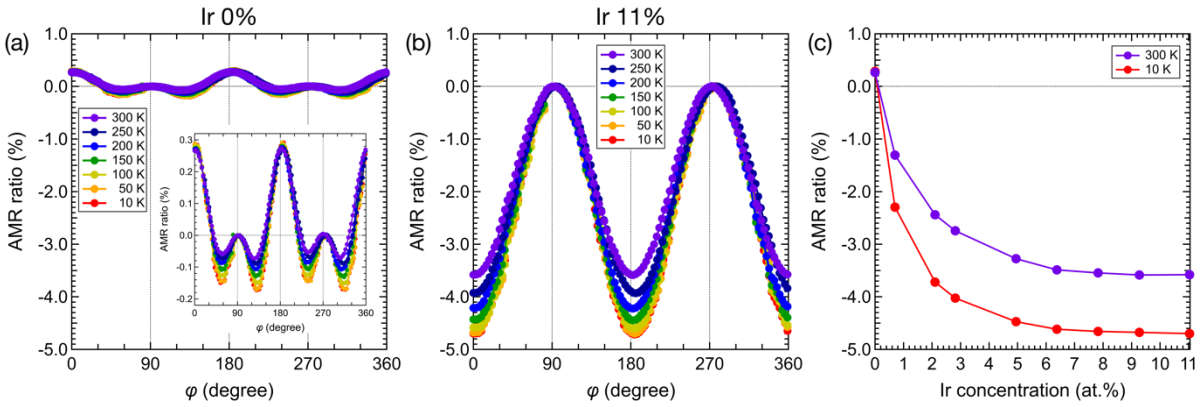

FIG. 6. (a) Temperature dependence on anisotropic magnetoresistance (AMR) ratio of $(Fe_3Co)_{100-x}Ir_x$ composition-spread thin films (a) without Ir (x = 0%) and (b) with x = 11%. The inset in part (a) shows the magnified view of the graph. (c) Compositional dependence on AMR ratio of the films measured at 10 and 300 K.

C. Theoretical analysis for negative AMR

We discuss the experimental AMR ratio upon Ir addition by the theoretical model using Eq. (3). This model considers *s*–*d* scattering of conduction electrons from *s* to *d* orbitals and crystal field in the *d* orbitals of the matrix material under a two-current model. For simplicity of the model, we choose *d* electrons of a single atom in a sublattice of one unit cell as the scattering destination in the *s*–*d* scattering process, where the atom has the largest contribution to the *s*–*d* scattering. The PDOS for the ε and γ orbitals of the *d* states of Fe, Co, and Ir atoms in *A*2-disordered Fe_3Co, *A*2-disordered $(Fe_3Co)_{89}Ir_{11}$, and *B*2-ordered $(Fe_3Co)_{89}Ir_{11}$ are shown in Figs. S3–S5 [48], respectively. The *a* values and atomic site occupancy for those structures used for the theoretical calculation are summarized in Table S□ [48]. Here, we choose x = 11% to study the negative AMR because the highest S_{B2} was obtained [Fig. 2(d)], the largest negative AMR ratio was observed [Fig. 6(c)], and the accurate structural analysis by STEM was performed for x = 11% (Fig. 5), which enables us to reproduce the experimental case reasonably. It is noted that we considered the ideal *B*2-ordered Fe_3Co–Ir structure in our calculation, as shown in Fig. 5(d). To choose a single atom of scattering destination, we compare the PDOS of *d* states of spin-down at E_F (*d*-DOS$_-$) for each atom at each site. If the *d*-DOS$_-$ is larger, the contribution to *s*–*d* scattering rate, thus the AMR effect, becomes larger. We also compare the smaller Δ or H value for each atom at each site. If the Δ or H value is smaller, the contribution to *s*–*d* scattering rate, thus the AMR effect, becomes larger because the *d* orbitals are distorted as the λ/Δ or λ/H increases. The *d*-DOS$_-$, Δ, and H values for each atom at each site of the three structures are summarized in Table S□ [48]. From the comparison of those values for each structure in accordance with the above guideline, we consider the *d* orbitals of Fe atoms at 1*a* site as the dominant *s*–*d* scattering process for all three structures (see the explanation in Table S□ for detail [48]).

We estimate the values for parameters used in Eq. (3). From the first-principles calculation (Figs. S3–S5 [48]), we confirmed that the values for $D_+^{(s)}$, $D_-^{(s)}$, and $D_{\varepsilon,-}^{(d)}$ were almost independent to the materials. Thus, these parameters were fixed by their average values as $D_+^{(s)}$ = 0.009, $D_-^{(s)}$ = 0.003, and $D_{\varepsilon,-}^{(d)}$ = 0.05. In contrast, the values for Δ and $D_{\gamma,-}^{(d)}$ depended largely on the materials. Thus, Δ and $D_{\gamma,-}^{(d)}$ were treated as variables. The m_-^*/m_+^* value was estimated from the calculated energy dispersion diagrams of the conduction electrons with spin-up and spin-down states. The energy difference from the valence band maximum or conduction band minimum in spin-up (-down) state can be expressed as $\Delta E_{+(-)} = \frac{(\hbar k)^2}{2m_{+(-)}^*}$, where $\hbar$ is the Planck constant and k is the magnitude of the wave vector. When considering the same k value for both spin-up and spin-down states, we obtained $\frac{m_-^*}{m_+^*} = \frac{\Delta E_+}{\Delta E_-} \approx 0.5$. Considering the possibility of error, the calculation of AMR ratio was performed with the m_-^*/m_+^* value ranging from 0.3 to 0.5. The remaining parameters were fixed as λ = 0.052 eV [54], H = 3 eV (Table S□), and $\beta_{+(-)}$ = 0.1 [55].

Here, we introduce a parameter $\left(D_{\gamma,-}^{(d)} - D_{\varepsilon,-}^{(d)}\right)/D_{\varepsilon,-}^{(d)}$ to explain the sign change of AMR ratio,

where the $D_{\varepsilon,-}^{(d)}$ value is set to be 0.05. Because the magnitude relationship between $D_{\gamma,-}^{(d)}$ and $D_{\varepsilon,-}^{(d)}$ is crucial to determine the sign of AMR ratio [41,42], it is useful to investigate the behavior of AMR ratio with respect to this parameter.

The dependence of $\left(D_{\gamma,-}^{(d)} - D_{\varepsilon,-}^{(d)}\right)/D_{\varepsilon,-}^{(d)}$ on normalized theoretical AMR ratio for $\Delta = 0.6$ and 2 eV is shown in Fig. 7. The Δ values were estimated to 0.6 eV for *B*2-ordered $(Fe_3Co)_{89}Ir_{11}$ and 2 eV for *A*2-disordered Fe_3Co and *A*2-disordered $(Fe_3Co)_{89}Ir_{11}$ (Table S□ [48]). From the first-principles calculation, the $\left(D_{\gamma,-}^{(d)} - D_{\varepsilon,-}^{(d)}\right)/D_{\varepsilon,-}^{(d)}$ values were estimated to 0.031 for *B*2-ordered $(Fe_3Co)_{89}Ir_{11}$, –0.44 for *A*2-disordered $(Fe_3Co)_{89}Ir_{11}$, and –0.53 for *A*2-disordered Fe_3Co, which are indicated in Fig. 7.

The dependence of $\left(D_{\gamma,-}^{(d)} - D_{\varepsilon,-}^{(d)}\right)/D_{\varepsilon,-}^{(d)}$ on each term in normalized theoretical AMR ratio in the right-hand side of the Eq. (3) for $\Delta = 0.6$ eV and $\Delta = 2$ eV with $m_-^*/m_+^* = 0.3$ is shown in Fig. S6 [48]. For each structure, the AMR ratio depends mainly on the 1st term in the right-hand side of the equation (3) $\left[\left(\frac{\lambda}{\Delta}\right)^2\left(r_{s,-\to\varepsilon,-} - r_{s,-\to\gamma,-}\right)\right]$. As a qualitative explanation, because the 1st term is proportional to $\left(\frac{\lambda}{\Delta}\right)^2\left(D_{\varepsilon,-}^{(d)} - D_{\gamma,-}^{(d)}\right)$, the sign of AMR ratio becomes positive for almost all region of $D_{\gamma,-}^{(d)} < D_{\varepsilon,-}^{(d)}$ and negative for almost all region of $D_{\gamma,-}^{(d)} > D_{\varepsilon,-}^{(d)}$. The absolute value of AMR ratio becomes larger as the Δ value becomes smaller. Especially, the AMR ratio becomes a larger negative value as increasing the $\left(D_{\gamma,-}^{(d)} - D_{\varepsilon,-}^{(d)}\right)/D_{\varepsilon,-}^{(d)}$ value.

From the PDOS of Fe at 1*a* site for *B*2-ordered $(Fe_3Co)_{89}Ir_{11}$ in Fig. S4 [48], we find the relation $D_{\varepsilon,-}^{(d)} < D_{\gamma,-}^{(d)}$. Considering of Δ = 0.6, the AMR ratio for *B*2-ordered $(Fe_3Co)_{89}Ir_{11}$ became a large negative (red curves in Fig. 7), which is consistent with the experimental results as shown in Fig. 6. In contrast, because of the relation $D_{\varepsilon,-}^{(d)} > D_{\gamma,-}^{(d)}$ for *A*2-disordered Fe_3Co and *A*2-disordered $(Fe_3Co)_{89}Ir_{11}$ (Figs. S2 and S3 [48]) and the larger Δ value of 2 eV, their AMR ratios became a small positive (blue curves in Fig. 7). As a result, a large negative AMR ratio of *B*2-ordered $(Fe_3Co)_{89}Ir_{11}$ was obtained by the theoretical model. Thus, our theoretical analysis qualitatively agrees with the experimentally observed AMR ratios in terms of their sign and magnitude correlation.

Although the negative AMR was successfully reproduced for the *B*2-ordered $(Fe_3Co)_{89}Ir_{11}$, there is limitation in the current theoretical model of this study to explain the negative AMR for lower Ir concentration and the saturation behavior of AMR ratio from x = 6.4% [Fig. 6(c)]. We also calculated PDOS and theoretical AMR ratio for x lower than 11% with the *B*2-ordered structure. As a result, the theoretical AMR ratio for x = 9.3% was negative (Fig. S7 [48]), which agrees with the experimental results [Fig. 6(c)]. In contrast, the theoretical AMR ratio became positive for x lower than 9.3% such as 7.8%, 6.4%, and 0.7%. Thus, the experimentally observed negative AMR ratio for the low Ir concentrations ($x \leqq 7.8\%$) could not be reproduced. We consider the reason of this discrepancy for the low Ir concentration as follows: the current theoretical model assumes that the lattice including Ir atom

is the matrix material and that electrons are scattered by impurities (*e.g.*, light elements) as scatterers. On the other hand, for the low Ir concentration, which can be regarded as a diluted Ir material rather than the matrix material including Ir, it would be necessary to consider Ir atom itself as a scatterer, and this effect is not included in the current theoretical model. Thus, the negative AMR for the low Ir concentration ($x \leqq 7.8\%$), as well as the saturation behavior of AMR ratio, could not be reproduced.

Consequently, the sign change of AMR ratio from positive to negative upon *B*2-ordering of Ir-doped Fe_3Co films for the high Ir concentration ($x \geqq 9.3\%$) reproduced by the theoretical model suggests that the metastable *B*2-ordering would be the key to observe the negative AMR.

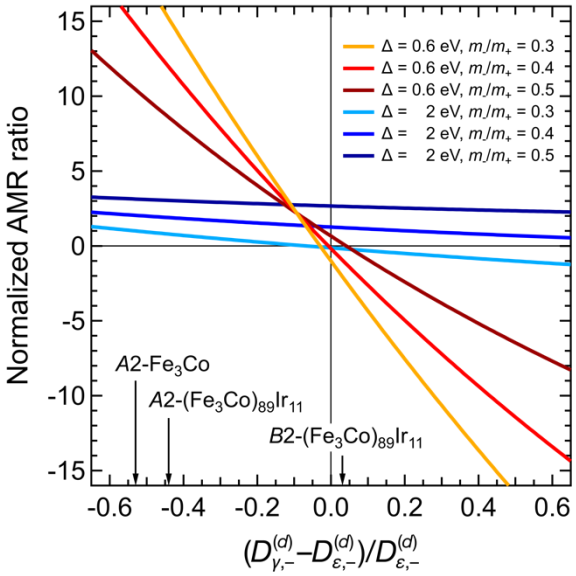

FIG. 7. The dependence of $\left(D^{(d)}_{\gamma,-} - D^{(d)}_{\varepsilon,-}\right)/D^{(d)}_{\varepsilon,-}$ on normalized theoretical AMR ratio for $\Delta = 0.6$ eV [*B*2-ordered $(Fe_3Co)_{89}Ir_{11}$] and $\Delta = 2$ eV [*A*2-disordered Fe_3Co and *A*2-disordered $(Fe_3Co)_{89}Ir_{11}$]. The $\left(D^{(d)}_{\gamma,-} - D^{(d)}_{\varepsilon,-}\right)/D^{(d)}_{\varepsilon,-}$ values were estimated to 0.031 for *B*2-ordered $(Fe_3Co)_{89}Ir_{11}$, –0.44 for *A*2-disordered $(Fe_3Co)_{89}Ir_{11}$, and –0.53 for *A*2-disordered Fe_3Co from the first-principles calculation.

□. CONCLUSIONS

We observed a large negative AMR ratio in Fe_3Co single-crystal thin films upon Ir addition and elucidated its origin by a theoretical model. $(Fe_3Co)_{100-x}Ir_x$ composition-spread thin films with x up to 11% were fabricated on MgO(100) substrates using combinatorial sputtering technique, and the Ir concentration dependence on the AMR effect was investigated. From the laboratory and synchrotron XRD results, superlattice peaks corresponding to Fe_3Co–Ir *100* and *111* with spot-like shapes were detected in the films with x from 2.1%, which indicates the formation of metastable *B*2-ordered Fe_3Co–Ir single-crystal thin films. The cross-sectional HAADF-STEM images and NBED patterns of the region with $x = 11\%$ also confirmed the [001]-oriented epitaxial growth and the *B*2-ordering of Fe_3Co–Ir. From the EDS results, the characteristic atomic site occupancy in the metastable *B*2-ordered structure was

confirmed; the Fe- and Co-columns tended to be arranged alternatively and the Ir atoms tended to occupy the Co sites preferentially. From the AMR measurement, the pure Fe_3Co (without Ir) showed a small positive AMR ratio of 0.3%. In contrast, once the Ir atoms were added, the AMR ratio became negative, and it exhibited the largest negative values of –4.7% at 10 K and –3.6% at 300 K for x = 11%. Using a theoretical model, a small positive and a large negative AMR ratio of *A*2-disordered Fe_3Co and *B*2-ordered Ir-doped Fe_3Co were obtained, respectively, which was consistent with the experimental results qualitatively. Moreover, the sign of calculated AMR ratio of *A*2-disordered Ir-doped Fe_3Co showed positive. The sign change of AMR ratio from positive to negative upon *B*2-ordering of Ir-doped Fe_3Co films reproduced for the high Ir concentration ($x \geqq 9.3\%$) by the theoretical model suggests that the metastable *B*2-ordering would be the key to observing the negative AMR. These findings provide a deep insight into the origin of AMR in heavy-metal-doped ferromagnetic ordered alloys.

ACKNOWLEDGMENTS

The authors thank T. Hiroto and T. Nakatani for the technical support with the XRD measurements. The synchrotron XRD measurement was performed with the approval of Japan Synchrotron Radiation Research Institute (Proposal No. 2023A1563). This work was supported by JSPS KAKENHI (Grant No. 19K05249), JST CREST (Grant No. JPMJCR21O1), and MEXT Program: Data Creation and Utilization-Type Material Research and Development Project (Digital Transformation Initiative Center for Magnetic Materials; Grant No. JPMXP112271), Japan.

REFERENCES

[1] T. R. McGuire and R. I. Potter, *IEEE Trans. Magn.* **MAG-11**, 1018 (1975).

[2] C.-J. Zhao, L. Ding, J.-S. HuangFu, J.-Y. Zhang, and G.-H. Yu, *Rare Met.* **32**, 213 (2013).

[3] J. Smit, *Physica* **17**, 612 (1951).

[4] T. T. Chen and V. A. Marsocci, *J. Appl. Phys.* **43**, 1554 (1972).

[5] M. Inagaki, M. Suzuki, Y. Iwama, and U. Mizutani, *Jpn. J. Appl. Phys.* **25**, 1514 (1986).

[6] Th. G. S. M. Rijks, S. K. J. Lenczowski, R. Coehoorn, and W. J. M. de Jonge, *Phys. Rev. B* **56**, 362 (1997).

[7] R. P. van Gorkom, J. Caro, T. M. Klapwijk, and S. Radelaar, *Phys. Rev. B* **63**, 134432 (2001).

[8] W. Gil, D. Görlitz, M. Horisberger, and J. Kötzler, *Phys. Rev. B* **72**, 134401 (2005).

[9] B. G. Tóth, L. Péter, Á. Révész, J. Pádár, and I. Bakonyi, *Eur. Phys. J. B* **75**, 167 (2010).

[10] I. Turek, J. Kudrnovský, and V. Drchal, *Phys. Rev. B* **86**, 014405 (2012).

[11] L. K. Zou, Y. Zhang, L. Gu, J. W. Cai, and L. Sun, *Phys. Rev. B* **93**, 075309 (2016).

[12] Y. Yang, Z. Luo, H. Wu, Y. Xu, R.-W. Li, S. J. Pennycook, S. Zhang, and Y. Wu, *Nat. Commun.* **9**, 2255 (2018).

[13] M. W. Jia, J. X. Li, H. R. Chen, F. L. Zeng, X. Xiao, and Y. Z. Wu, *New J. Phys.* **22**, 043014 (2020).

[14] F. L. Zeng, Z. Y. Ren, Y. Li, J. Y. Zeng, M. W. Jia, J. Miao, A. Hoffmann, W. Zhang, Y. Z. Wu, and Z. Yuan, *Phys. Rev. Lett.* **125**, 097201 (2020).

[15] H. C. Van Elst, *Physica* **25**, 708 (1959).

[16] T. R. McGuire, J. Aboaf, and E. Klokholm, *J. Appl. Phys.* **53**, 8219 (1982).

[17] T. Miyazaki, T. Ajima, and F. Sato, *J. Magn. Magn. Mater.* **83**, 111 (1990).

[18] T. Tanaka, I. Kobayashi, M. Takahashi, and T. Wakiyama, *IEEE Trans. Magn.* **26**, 2418 (1990).

[19] M.-M. Chen, N. Gharsallah, G. L. Gorman, and J. Latimer, *J. Appl. Phys.* **69**, 5631 (1991).

[20] S. U. Jen, *Phys. Rev. B* **45**, 9819 (1992).

[21] H. Nagura, K. Saito, K. Takanashi, and H. Fujimori, *J. Magn. Magn. Mater.* **212**, 53 (2000).

[22] S. Wimmer, D. Ködderitzsch, and H. Ebert, *Phys. Rev. B* **89**, 161101(R) (2014).

[23] Y. Hsu, S. Jen, and L. Berger, *J. Appl. Phys.* **50**, 1907 (1979).

[24] J. Kudrnovský, V. Drchal, S. Khmelevskyi, and I. Turek, *Phys. Rev. B* **84**, 214436 (2011).

[25] J. Kudrnovský, V. Drchal, and I. Turek, *J. Supercond. Nov. Magn.* **26**, 1749 (2013).

[26] J. Kudrnovský, V. Drchal, and I. Turek, *Phys. Rev. B* **89**, 224422 (2014).

[27] J. Kudrnovský, V. Drchal, and I. Turek, *Phys. Rev. B* **92**, 224421 (2015).

[28] T. Seki, S. Kikushima, and K. Takanashi, *J. Magn. Soc. Jpn.* **43**, 29 (2019).

[29] Y. Dai, Y. W. Zhao, L. Ma, M. Tang, X. P. Qiu, Y. Liu, Z. Yuan, and S. M. Zhou, *Phys. Rev. Lett.* **128**, 247202 (2022).

[30] O. Jaoul, I. A. Campbell, and A. Fert, *J. Magn. Magn. Mater.* **5**, 23 (1977).

[31] T. R. McGuire, J. A. Aboaf, and E. Klokholm, *IEEE Trans. Magn.* **MAG-20**, 972 (1984).

[32] S. Senoussi, I. A. Campbell, and A. Fert, *Solid State Commun.* **21**, 269 (1997).

[33] Y. Iwasaki, R. Sawada, E. Saitoh, and M. Ishida, *Commun. Mater.* **2**, 31 (2021).

[34] H. Koinuma and I. Takeuchi, *Nat. Mater.* **3**, 429 (2004).

[35] J.-C. Zhao, *Prog. Mater. Sci.* **51**, 557 (2006).

[36] Z. H. Barber and M. G. Blamire, *Mater. Sci. Technol.* **24**, 757 (2008).

[37] A. Ludwig, R. Zarnetta, S. Hamann, A. Savan, and S. Thienhaus, *Int. J. Mat. Res.* **99**, 1144 (2008).

[38] R. Modak, K. Goto, S. Ueda, Y. Miura, K. Uchida, and Y. Sakuraba, *APL Mater.* **9**, 031105 (2021).

[39] S. P. Padhy, Z. Tsakadze, V. Chaudhary, G. J. Lim, X. Tan, W. S. Lew, and R. V. Ramanujan, *Res. Mater.* **14**, 100283 (2022).

[40] K. Momma and F. Izumi, *J. Appl. Cryst.* **44**, 1272 (2011).

[41] S. Kokado and M. Tsunoda, *J. Phys. Soc. Jpn.* **88**, 034706 (2019).

[42] T. Sato, S. Kokado, M. Tsujikawa, T. Ogawa, S. Kosaka, M. Shirai, and M. Tsunoda, *Appl. Phys. Express* **12**, 103005 (2019).

[43] T. Sato, S. Kokado, H. Shinya, M. Tsujikawa, A. Miura, S. Kosaka, T. Ogawa, M. Shirai, and M. Tsunoda, *J. Appl. Phys.* **132**, 223907 (2022).

[44] J. Korringa, *Physica* **13**, 392 (1947).

[45] W. Kohn and N. Rostoker, *Phys. Rev.* **94**, 1111 (1954).

[46] http://kkr.issp.u-tokyo.ac.jp/

[47] J. P. Perdew, K. Burke, and M. Ernzerhof, *Phys. Rev. Lett.* **77**, 3865 (1996).

[48] See Supplemental Material at [URL will be inserted by publisher] for the 2D XRD images of the films; the synchrotron XRD pattern of the region with $x = 0\%$; the PDOS for $A2$-disordered Fe_3Co, $A2$-disordered $(Fe_3Co)_{89}Ir_{11}$, $B2$-ordered $(Fe_3Co)_{90.7}Ir_{9.3}$, and $B2$-ordered $(Fe_3Co)_{89}Ir_{11}$; the a values and atomic site occupancy for those structures used for the theoretical calculation; the explanation for choosing d electrons of a single atom as the scattering destination in the s–d scattering process; the dependence of $\left(D_{\gamma,-}^{(d)} - D_{\varepsilon,-}^{(d)}\right)/D_{\varepsilon,-}^{(d)}$ on each term in normalized theoretical AMR ratio in the right-hand side of the Eq. (3); and the dependence of $\left(D_{\gamma,-}^{(d)} - D_{\varepsilon,-}^{(d)}\right)/D_{\varepsilon,-}^{(d)}$ on normalized theoretical AMR ratio.

[49] H. Asano, Y. Bando, N. Nakanishi, and S. Kachi, *Trans. Jpn. Inst. Met.* **8**, 180 (1967).

[50] O. F. Polkopina and V. V. Kuprina, *Fazovye Ravnovesiya Met. Splavakh*, 277 (1981).

[51] K. Kabara, M. Tsunoda, and S. Kokado, *AIP Adv.* **6**, 055818 (2016).

[52] S. Kokado and M. Tsunoda, *J. Phys. Soc. Jpn.* **84**, 094710 (2015).

[53] S. Kokado and M. Tsunoda, *J. Phys. Soc. Jpn.* **91**, 044701 (2022).

[54] S. Kokado and M. Tsunoda, *J. Phys. Soc. Jpn.* **88**, 068001 (2019).

[55] S. Kokado, Y. Sakuraba, and M. Tsunoda, *Jpn. J. Appl. Phys.* **55**, 108004 (2016).